Preliminary investigation of the electromagnetic fields in the far plume of a Helicon Plasma Thruster

P.Jiménez, M.Merino, E.Ahedo

Equipo de Propulsión Espacial y Plasmas, Universidad Carlos III de Madrid, Leganés, Spain,
pejimene@ing.uc3m.es

Abstract:

An efficient radiofrequency power coupling is one of the main challenges that remain to be solved in the operation of Helicon Plasma Thrusters (HPTs). This work presents an extension to previous coupled plasma transport and plasma-wave simulations to account for the power deposition in the plasma plume and surroundings of the thruster. Plasma profiles in the source are found from the coupled simulations using the HYPHEN platform. A different methodology, assuming a collisionless expansion in the magnetic nozzle downstream, is used to find the plasma density and collision frequency in the far plume. The electromagnetic fields are obtained using a full-wave cold magnetised plasma model. The effect of the Electron Cyclotron Resonance and the changes in the power deposition profiles are studied.

1. INTRODUCTION

Helicon Plasma Thrusters (HPTs) are novel electric propulsion devices currently under research and testing. The operation of these thrusters relies on the plasma heating in a Helicon source and the later acceleration of the plasma in a magnetic nozzle [1]. HPTs would offer notable advantages compared to traditional electric propulsion technologies such as Gridded Ion Thrusters or Hall Effect Thrusters. The lack of electrodes limits the erosion of the engine resulting on enhanced lifetime and the possibility of easily using alternative propellants. Furthermore, the easy control of the power input and magnetic nozzle topology allow for a high throttlability.

However, there are still open challenges in the design and optimization of HPTs, particularly, the low thruster efficiency, still under 20% [2]. One of the critical phenomena in the operation of the thruster is the radiofrequency (RF) power coupling between the helical antenna and the plasma source.

While there have been advances in the recent years [3] in the modeling of the electromagnetic fields in the plasma discharge, work is still needed to understand wave propagation and absorption in the whole device, including the far-region plasma plume, the effect of metallic components and the tenuous plasma in the source surroundings.

The EP2 research group has developed the 2D asymmetric simulation tool HYPHEN. This code is meant to become a powerful multi-thruster simulation platform with applications for different devices [4], [5]. HYPHEN uses a hybrid approach comprising a PIC module for heavy species and a fluid model for electrons in order to solve the complete plasma discharge.

Recently, an electromagnetic full-wave solver module has been added to HYPHEN aiming at solving self-consistently the plasma transport and antenna coupling in electrodeless thrusters. For such simulations integrating the power deposited by the waves in the plasma and the evolution of the plasma dynamics due to electromagnetic heating, the usual strategy is to consider that the plasma is static as seen by the fast oscillating electromagnetic fields. This is done on account of the long resident time of the particles within the plasma compared to the high excitation frequency in the RF or microwave range. The group presented two examples of integrated simulations in the 36th International Electric Propulsion Conference (IEPC) both using the hybrid HYPHEN code for the plasma dynamics with a FEM 2D axisymmetric wave propagation code for Electron Cyclotron Resonance devices [6] and a 2D FD code with azimuthal modes for the HPT [7]. The later, named PYEE, will continue to be employed for HPTs simulations considering the better numerical behavior at moderate to low antenna frequencies and its capability to solve any azimuthal mode.

Up to know the HYPHEN domain extension has been limited to the thruster's tube and a small fraction of the plume. The objective of this paper is to asses the influence of the plume in the electromagnetic power deposition. To accomplish this goal, the previous domain will be extended. The domain enlargement is of paramount importance due to the existence of an Electron Cyclotron Resonance surface far downstream, where the magnetic field strength is sufficiently low for the resonance conditions to be

met. This transition affects the wave propagation and plays an important role in the electromagnetic power confinement.

The plasma density and effective electron collision frequencies are obtained in the thruster's tube and near plume from the stationary solution of the coupled HYPHEN-PYEE simulations. These profiles come from simulations launched in what we will call the small domain.

The plasma profiles in the region of the plume outside the small domain are not known a priori. The supersonic plasma acceleration in the magnetic nozzle is computed from the plasma profiles at the edge of the HYPHEN domain using the DIMAGNO code [8]. The model used for this simulation assumes a collisionless, electron-magnetized, low-beta, current-free plasma.

Finally, for the sake of a better modeling of the operation of the thruster inside the vacuum chamber, the metallic walls serving as boundary conditions to the full-wave solver are moved away from the thruster. Internal metallic boxes, modeling equipment such as the coils used to generate the background magnetic field, are also new features since the first coupled simulations [9]. Due to numerical concerns caused by the very small-scale structures appearing near the ECR line, the collisionality has been scaled up. This is intended to damp short wave-length noise while not changing dramatically the overall power deposition map. This issue will be tackle in future simulations.

The wave solution in this work is not fed back to the transport code and iterated until a self-consistent solution is achieved. However, the analysis presented below already shows interesting insight into several key aspects of the electromagnetic fields in the HPT.

The rest of this paper is structured as follows. Section 2 describes the plasma-wave model used for the full-wave simulations. Section 3 explains the discretization and numerical implementation of such model. Section 4 presents the simulation setup and the different sub-domains considered. Section 5 is a discussion of the electromagnetic wave and power deposition profiles obtained in the simulations. A discussion on the convergence and the contribution of secondary modes is also included.

2. 2D PLASMA-WAVE MODEL

The propagation of electromagnetic waves inside the thruster and vacuum chamber is governed by Maxwell's equations:

$$\nabla \cdot \boldsymbol{E} = \frac{\rho}{\varepsilon_0}, \qquad \text{(Eq. 1)}$$

$$\nabla \times \boldsymbol{E} = -\frac{\partial \boldsymbol{B}}{\partial t}, \qquad \text{(Eq. 2)}$$

$$\nabla \cdot \boldsymbol{B} = 0, \qquad \text{(Eq. 3)}$$

$$c^2 \nabla \times \boldsymbol{B} = \frac{\boldsymbol{j}}{\varepsilon_0} + \frac{\partial \boldsymbol{E}}{\partial t}. \qquad \text{(Eq. 4)}$$

Due to the presence of charged particles within the plasma, the current term should include both the plasma electric current density and the external excitation in the antenna $\boldsymbol{j} = \boldsymbol{j}_p + \boldsymbol{j}_a$. Considering the cylindrical symmetry of the setup, and looking for the steady state physics of the device, any electromagnetic field can be written as the product of a complex magnitude that depends only on the radial and axial coordinates and a exponential phasor:

$$\boldsymbol{A}(z, r, \theta, t) = \tilde{\boldsymbol{A}}(z, r) \exp(im\theta - i\omega t),$$

where $m \in \mathbf{N}$ is the azimuthal wavenumber and $\omega = 2\pi f$ is the antenna angular excitation frequency. From now on we will work with these complex magnitudes labeled as $(E_z, E_r, E_\theta, B_z, B_r, B_\theta)$.

2.1. Cold plasma dielectric tensor

The macroscopic effect of the plasma currents is captured by a modification of the effective electric field in Ampere's Law (Eq. 4):

$$\nabla \times \boldsymbol{B} = \mu_0 \left(\boldsymbol{j}_a + \frac{\partial \boldsymbol{D}}{\partial t} \right), \qquad \text{(Eq. 5)}$$

where the electric displacement field $\boldsymbol{D}$ is:

$$\boldsymbol{D} = \varepsilon_0 \boldsymbol{E} + \frac{\mathrm{i}\boldsymbol{j}_p}{\omega} = \varepsilon_0 \overline{\overline{\kappa}}(z, r) \cdot \boldsymbol{E} \qquad \text{(Eq. 6)}$$

The last expression assumes that there exist a linear relation between the electric and displacement fields. The second order dielectric tensor $\overline{\overline{\kappa}}$ can be found from the charged particle momentum equation under two assumptions [10]:

1. The thermal/pressure term is much weaker than the wave induced electromagnetic forces.

2. The externally applied magnetic field is static and much stronger than the wave induced magnetic field.

Selecting a right handed orthonormal coordinate system with the static magnetic field directed along the z-direction $\boldsymbol{B}_0 = B_0 \mathbf{1}_{\boldsymbol{z}}$, the dielectric tensor takes the form [10]

$$\overline{\overline{\kappa}}(z, r) = \begin{pmatrix} S & -iD & 0 \\ iD & S & 0 \\ 0 & 0 & P \end{pmatrix} \qquad \text{(Eq. 7)}$$

with:

$$S \equiv \frac{1}{2}(R + L) \tag{Eq. 8}$$

$$D \equiv \frac{1}{2}(R - L) \tag{Eq. 9}$$

$$P \equiv 1 - \sum_s \frac{\omega_{ps}^2}{\omega(\omega + i\nu_m)} \tag{Eq. 10}$$

$$R \equiv 1 - \sum_s \frac{\omega_{ps}^2}{\omega(\omega + i\nu_m + \omega_{cs})} \tag{Eq. 11}$$

$$L \equiv 1 - \sum_s \frac{\omega_{ps}^2}{\omega(\omega + i\nu_m - \omega_{cs})} \tag{Eq. 12}$$

and:

$$\omega_{cs}(z, r) = \frac{Z_s e B_0}{m_s}, \qquad \omega_{ps}^2(z, r) = \frac{n_s(Z_s e)^2}{m_s \varepsilon_0}. \tag{Eq. 13}$$

Above s denotes any charged species. Due to the considerably higher mobility, it is known that electrons play the most important role in the wave propagation phenomena at moderate and high excitation frequencies. Accordingly $Z_s = -1$ and the electron cyclotron and plasma frequencies become the main plasma parameters in the problem neglecting any other species contribution. The dielectric tensor is rotated at each point of the domain to be align with the magnetic field.

2.2. Model equations

In order to solve for the 9 electromagnetic fields, Faraday's and modified Ampere's law are used. This yields the following 6 scalar equations plus 3 additional equations from the constituent relation given in (Eq. 6):

$$\frac{im}{r}E_z - \frac{\partial}{\partial z}E_\theta - i\omega B_r = 0 \tag{Eq. 14}$$

$$\frac{\partial}{\partial z}E_r - \frac{\partial}{\partial r}E_z - i\omega B_\theta = 0 \tag{Eq. 15}$$

$$\frac{1}{r}\frac{\partial}{\partial r}(rE_\theta) - \frac{im}{r}E_r - i\omega B_z = 0 \tag{Eq. 16}$$

$$\frac{im}{r}B_z - \frac{\partial}{\partial z}B_\theta + i\omega\mu_0 D_r = \mu_0 j_{ar} \tag{Eq. 17}$$

$$\frac{\partial}{\partial z}B_r - \frac{\partial}{\partial r}B_z + i\omega\mu_0 D_\theta = \mu_0 j_{a\theta} \tag{Eq. 18}$$

$$\frac{1}{r}\frac{\partial}{\partial r}(rB_\theta) - \frac{im}{r}B_r + i\omega\mu_0 D_z = \mu_0 j_{az} \tag{Eq. 19}$$

Equation (Eq. 1) is satisfied if a charged conserving antenna current is imposed $\frac{\partial \rho}{\partial t} + \nabla \cdot \boldsymbol{j}_a = 0$. Correspondingly, any physical external magnetic field must comply with (Eq. 3).

2.3. Boundary conditions

To close the problem, a suitable set of boundary conditions must be enforced. For metallic walls, Perfect Electric Conductor (PEC) BCs are applied in all the boundaries besides the axis by imposing a null tangential field $\tilde{\boldsymbol{E}} \times \boldsymbol{n} = 0$. The staggered grid in Fig. 1 provides an easy implementation because the tangential fields lay precisely on the boundaries and, thus, the condition can be simply included as additional equations in the fully discretized system. When it comes to the axis, the application of BCs turns out to be more convoluted. The following conditions should be met to prevent the fields going to infinity and ensure continuity [11] (similar expressions are found for $\boldsymbol{B}$),

$$E_r^{(0)} = E_\theta^{(0)} = 0, \tag{Eq. 20}$$

$$E_r^{(\pm 1)} = \mp i E_\theta^{(\pm 1)}, \quad E_z^{(\pm 1)} = 0, \tag{Eq. 21}$$

$$E_r^{(m)} = E_\theta^{(m)} = E_z^{(m)} = 0 \quad |m| > 1. \tag{Eq. 22}$$

3. NUMERICAL IMPLEMENTATION

The numerical solution of the wave problem is obtained using a Finite Difference method, in particular, a modification of the well-known Yee staggered grid method [12], [13] to account for non-isotropic linear materials such as a cold magnetised plasma. Unlike the original leapfrog time marching Yee method, Maxwell's equations are solved in the frequency domain on account of the shortest wave propagation characteristic time when compared to the electron thermal velocity in the transport problem.
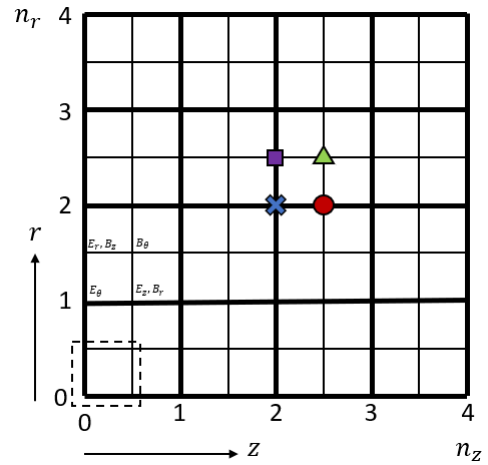

Figure 1: 2D staggered grid and electromagnetic fields. Each cell comprises a central node and four border nodes. E_θ is located in the blue X, E_z and B_r in the red circle, E_r and B_z in the purple square and finally B_θ in the green triangle.

The use of the staggered grid with alternating fields for the nodes inside a cell allows for an easy discretization of (Eq. 14) to (Eq. 19). The difference in the discretization with the vacuum Yee method arises from the need to estimate the value of the electric field in certain nodes where it is not solved for in the assembled system of equations. This requirement comes from the dielectric tensor times electric field product in the computation of the displacement field. A straightforward solution is to perform certain interpolations using nearby nodes where the electric field unknowns are placed [14].

The set of $6 \times n_z \times n_r$ equations (including boundary conditions) is assembled into the usual linear system form $A\boldsymbol{x} = \boldsymbol{b}$, where A is the matrix of coefficients and $\boldsymbol{b}$ is the forcing vector (antenna currents). A direct solver is applied to obtain the electric and magnetic field components contained in the solution vector $\boldsymbol{x}$. Averaging during a whole wave cycle $T = 2\pi/\omega$, the power deposited into the plasma reads $Q_a = \Re\left(\boldsymbol{j}_p^* \cdot \boldsymbol{E}/2\right)$, then the total power absorption can be computed as

$$P_a = \Re\left(\int_{V_p} \frac{\boldsymbol{j}_p^* \cdot \boldsymbol{E}}{2} \mathrm{d}V_p\right), \qquad \text{(Eq. 23)}$$

being V_p the volume comprising the plasma region. As a result of the linearity of the problem, it is possible to impose the total power deposited into the plasma and scale the fields and current through the antenna taking into account $P_{abs}^{1/2} \propto E \propto j_a \propto I_a$. Therefore, the antenna current and the plasma impedance can be obtained as outputs from the simulation. The scaled Q_a is given to the transport module which returns the updated plasma properties (density and collision frequency taking into account temperature).

4. SIMULATION SETUP

The device under simulation is the HPT05 Helicon Plasma Thruster developed by the EP2 team. The design parameters are displayed in Table 1.

The magnetic field is axial constituting the usual magnetic divergent nozzle with the throat located near the exit of the thruster tube. The HYPHEN simulation domain, featuring the main plasma source parameters and dimensions, is displayed in Fig.2.

As described in [15], the helical antenna can be modelled as a 3D current density expanded in azimuthal Fourier modes. An accurate simulation can be obtained as the sum of the arising fields from each of the modes obtained independently in 2D simulations. In light of previous studies [5], [14] showing that the vast majority of the plasma resistance corresponds to the interaction with the currents in the azimuthal mode $m = 1$, this mode

is used both in the HYPHEN simulations and the electromagnetic field profiles in the discussion section. Later, we perform an analysis of the power deposited in other modes.
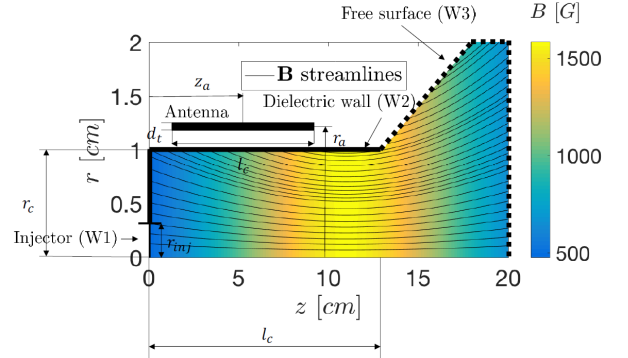

Figure 2: Small domain used for HYPHEN simulations and scheme of the HPT thruster dimensions (HPT05).

Parameter	
Wave Domain (rectangular)	$67\text{cm} \times 20\text{cm}$
Chamber length l_c	12.5 cm
Chamber radius r_c	1.25 cm
Propellant type	Xenon
Antenna type	Half-turn Helical
Antenna frequency f	13.56 MHz
Antenna Delivered Power	350 W
Antenna loop radius r_a	1.75 cm
Antenna length l_a	7.5 cm
Antenna central position z_a	7.5 cm
Antenna thickness d_t	0.05 cm
Reference magnetic field $B_{0,max}$	1500 G
Mass Flow $\dot{m}$	1 mg/s

Table 1: Simulation Parameters for the coupled simulations of the HPT05 thruster.

4.1. HYPHEN and DIMAGNO outputs

Plasma density and collision frequency profiles are output from the steady state solution of the coupled plasma-transport and plasma-wave interaction simulations on the small domain of Fig.2 (see [7]).

The wave domain is enlarged from the former HYPHEN domain to consider the plume expansion and the laboratory vacuum chamber. The DIMAGNO simulation domain starts immediately after the HYPHEN exit (free surface W3). The plume solution is found assuming an isothermal expansion and that electrons can move without colliding with other species as a result of the low density in this region. Note that collisions are important in

the much faster electron motion due to the rapidly oscillating electromagnetic fields rather than in the plasma transport problem. It is therefore neccesary to compute the effective electron collision frequency at the plume region which is estimated based on the temperature and plasma densities output by the DI-MAGNO simulation. It is observed that electron-ion (Coulomb) collisions clearly dominate at this area, $v_{ei} \sim n_e R_{ei}$ with,

$$R_{ei} = \left(\frac{1\text{eV}}{T_e}\right)^{3/2} \times \ln \Lambda \times 2.9 \cdot 10^{-12} \text{ m}^3 \text{ s}^{-1} \quad \text{(Eq. 24)}$$

and,

$$\ln \Lambda \approx 9 + \frac{1}{2} \ln \left[\left(\frac{10^{18} \text{ m}^{-3}}{n_e}\right)\left(\frac{T_e}{1\text{eV}}\right)^3\right] \quad \text{(Eq. 25)}$$

This model is also used for the rest of the vacuum chamber included in the wave domain which is filled with a tenuous plasma of density $10^{14} m^{-3}$, a value expected in vacuum chamber operation and comparable to the low density reached far downstream in the periphery of the magnetic nozzle. Observe that this value of the background plasma density yields a plasma frequency that is larger than the excitation frequency (13.56 MHz), and consequently the plasma is overdense everywhere, including outside of the source and the main plume. Incidentally, this has the additional advantage of removing the transition P=0 from the simulation, which is known to introduce spurious oscillations. Electron-neutral collisions, based on an estimation of the neutral density $n_n \approx 10^{16} \text{ m}^{-3}$ at the outer plume and chamber, are negligible compared to the e-i collisionality.

4.2. Plasma property profiles in the wave domain

The rectangular wave domain used in PYEE to solve for the 6 electromagnetic fields is shown in Figs.3,4,5. Notice that metalic boxes (PEC boundary conditions) are included and depicted in black in all the profiles. This is meant to improve the modelling of the actual thruster by accounting for the metallic material of both the coils used to generate the background magnetic field (central box) and the thruster backplate and equipment (rear box).

The next figures show the main plasma parameters governing the wave propagation phenomena, namely the electron cyclotron frequency, proportional to the magnetic field strength, the plasma density and the effective electron collision frequency.
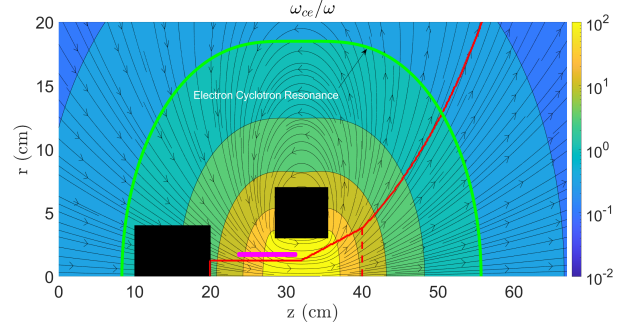

Figure 3: Electron cyclotron frequency ω_{ce}/ω and magnetic field lines. The antenna is shown in magenta and internal PEC boundaries in black.

The magnetic field strength decreases enough far from the coils to arrive to the Electron Cyclotron Resonance $\omega_{ce}/\omega = 1$. As it will be discussed later on, this feature has a profound influence in the electromagnetic power confinement.
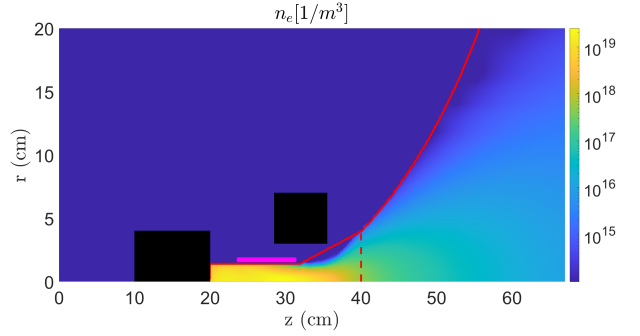

Figure 4: Plasma density n_e. The antenna is shown in magenta and internal PEC boundaries in black.
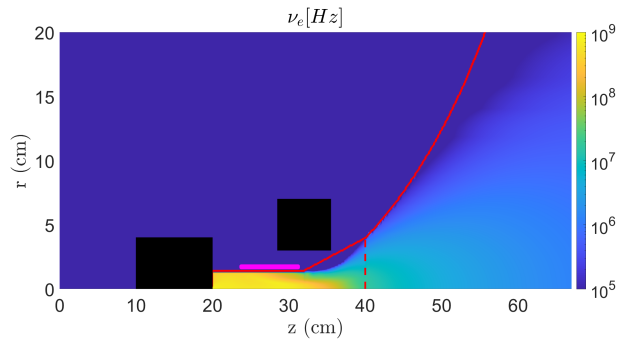

Figure 5: Effective electron collision frequency ν_e. The antenna is shown in magenta and internal PEC boundaries in black. The separation between HYPHEN and DIMAGNO domains is shown as a red dashed line.

The transition between the HYPHEN and DIMAGNO domains is achieved smoothly in the plasma density profile, Fig. 4. The plasma is denser in the thruster tube approaching $n_e = 10^{20} \text{ m}^{-3}$ near the backplate and axis. The density decays

rapidly in the divergent plume to values near $n_e = 10^{14}$ m^{-3}.

The matching between the collision frequencies at the HYPHEN domain (where neutral ellastic and inelastic collisions are considered) and the plume region is smooth thus validating the assumption that e-i collisions dominate downstream.

In this preliminary study, the collisionality map has been scaled up from nominal values to solve some concerns related to the simulation resolution, specially, near the ECR resonance where very short wave-length patterns tend to appear. It remains object of future work to decrease the collisionality and study the numerical convergence in that case.

5. RESULTS AND DISCUSSION

The results presented in the following section correspond to a PYEE wave simulation with a resolution of 1000×1000 cells. The total number of degrees of freedom is 36 million and the computation time was 6272 s.

5.1. Electromagnetic Solution

The norm of the electric field vector is displayed in Fig.6. The fields are stronger in the low density region out of the source and plume and remarkably, near the antenna. The fields are much lower in magnitude inside the dense plasma, showing that the they have difficulty penetrating into it.

There is a clearly detectable transition that appears as a boundary confining the stronger fields. This area is delimited by the Electron Cyclotron Resonance line displayed in Fig.3. Being the plasma overdense everywhere and the cyclotron frequency greater than the antenna excitation frequency, the only propagating electromagnetic mode inside the bubble is the right hand polarized whistler wave [10].

The whistler wave propagates both inside the denser plasma of the tube and plume and the region of the chamber with $\omega_{ce}/\omega > 1$. In spite of that, the field's topology changes abruptly. The chamber area features a diffuse pattern of stationary radiation reflecting back and forth on the ECR surface and the border of the dense plasma. The magnetic lines seem to guide the propagation of the waves, predominantly parallel to the background magnetic field vector (a usual behavior observed in the R wave with a very narrow resonance cone). The wave-length gets shorter and propagation has an important perpendicular component approaching the ECR resonance, beyond it, the fields become evanescence and no wave can propagate. On the other hand, the fields in the dense plasma present considerably longer wave-lengths.
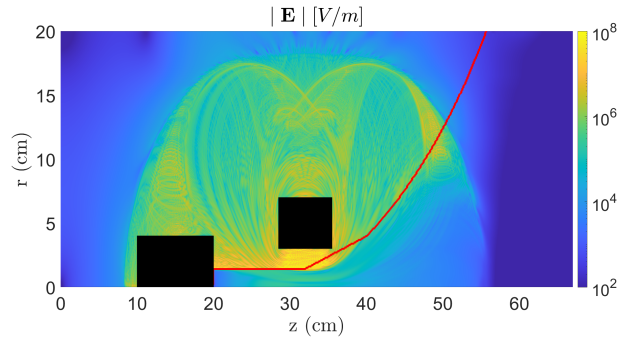

Figure 6: Electric field norm.

Regarding the power absorption profile in Fig.7, the power deposition is clearly maximum inside the source even though the fields are stronger out of it. This can be explained by the much denser plasma leading to an also greater collision frequency. Both effects sum up to a higher damping and power absorption.

The presence of two approximately symmetric arches surrounding the coils and reaching the proximity of the resonance might be explained by the fact that the power flux (Poynting's vector) becomes tangent to transition borders, thus creating a path from the antenna into higher density or otherwise inaccessible regions. This effect leads to a non-negligible heating downstream in the plume periphery.
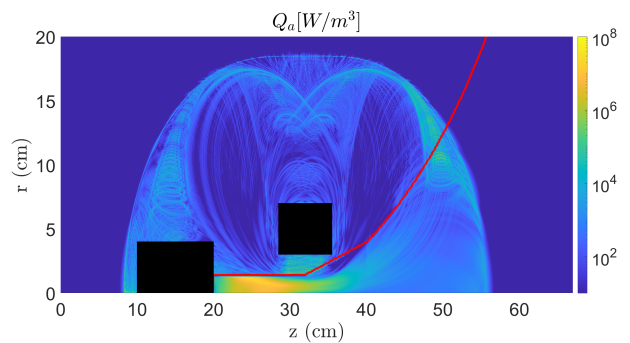

Figure 7: Power density.

Perhaps the most interesting feature in the power deposition profile, and not reported in previous works, is the role of the ECR as a very efficient electromagnetic power container. The preliminary simulations show that less than 0.6% of the total power emitted by the antenna is capable of escaping the bubble and reaching the metallic walls.

The transition observed in these results is particular to an overdense plasma [10]. The existence of the Electron Cyclotron Resonance only depends on the magnetic field strength and the antenna frequency but the behavior of the waves can vary as a function of the plasma density. The plasma is certainly overdense in the laboratory vacuum chamber

but this fact would be questionable in a space environment.

The overdense ECR transition will, in either case, appear downstream the plume and this effect introduces the possibility of considering it in the design of the magnetic field topology in order to increase the efficiency of HPTs devices.

5.2. Power map comparison

In order to asses the validity and accuracy of the coupled simulations carried out in previous works in a much smaller domain, it is interesting to compare the power deposition maps of both the small and extended cases. Figure 8 shows both profiles. Apart from the plume extension, the small domain does not feature the internal PEC boundary conditions, the limits of the bottom subplot are themselves perfect electric conductor walls.
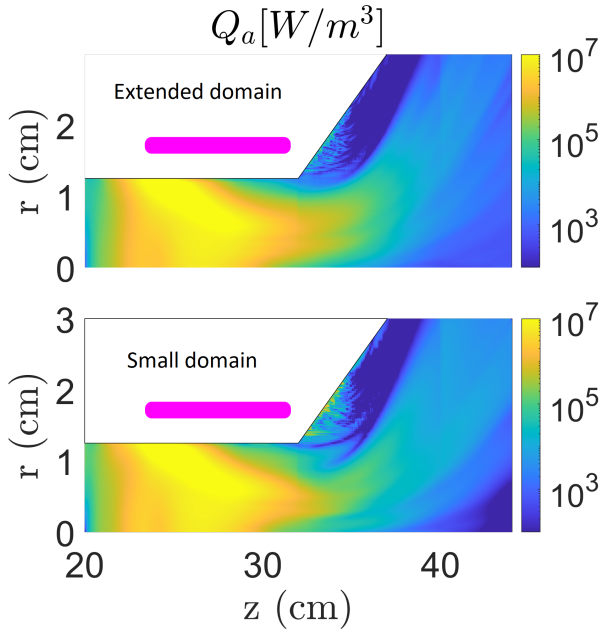

Figure 8: Power deposition in the tube and near plume for the extended and small simulation domains.

The straightforward conclusion from this study is that the solution inside the tube is mainly local and is not affected noticeably by the conditions in the far plume and chamber. However, although the power absorption map is not dramatically affected, the total power fraction deposited inside the thruster is greater in the small domain simulations (about 84%) than in the extended domain solution (close to 78%).

Interestingly, simulations carried out with a lower collision frequency showed that the actual fraction of power deposited in the plume could be much greater.

5.3. Higher azimuthal modes

Previous studies (see [3]) have shown that Nagoya III and helical antennas deposit most of the power in the azimuthal mode $m = 1$. This seems to hold at least for the case of Helicon sources. Accordingly, coupled simulations have been carried out considering only the dominant mode and, thus, saving the computational time required to compute the power absorption profiles for other modes. The results shown in Fig.9 unveil that, despite still being considerably lower than the total plasma resistance for $m = 1$, the addition of the plume and a larger domain make the contribution of the mode $m = -1$ quite significant. Notice that the half turn helical antenna only emits in odd mode numbers. Higher m values do not contribute significantly. A reasonable strategy for future coupled, self-consistent simulations could be to correct the steady state profiles considering both $m = 1$ and $m = -1$ for power deposition in the last iterations of the transport solver.
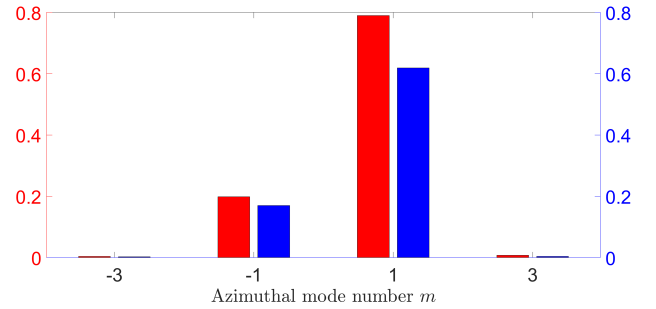

Figure 9: Fraction of total power (red) and fraction of power deposited inside the source (blue) for different azimuthal mode numbers, m.

5.4. Convergence and power by region

Figure 10 shows the fraction of power deposited in each region of the simulation domain as a function of the degrees of freedom in the linear system. The lines seem to stabilize with about 30 million DOFs. This indicates that the resolution of the mesh is capable of resolving the smallest length scales in the problem for the given density and collision frequency maps.

The results for the finest mesh show that more than 70% of the power is deposited inside the source while the rest is lost in the chamber and plume.
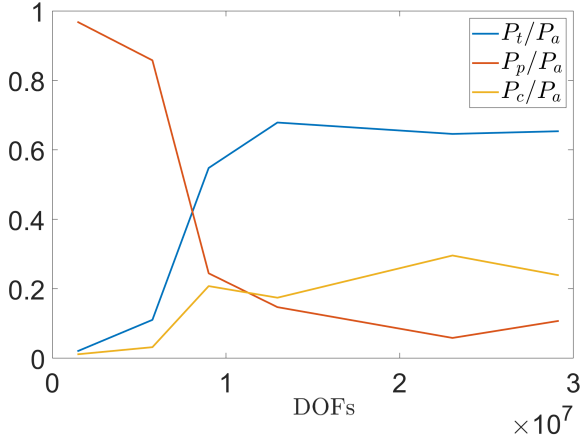
Figure 10: Fraction of power deposited in each region (blue tube, yellow chamber, red plume).

6. CONCLUSIONS

Full-wave simulations have been carried out in a domain about 3 times the length and 4 times the radius larger than the one in previous self-consistent plasma transport and EM wave interaction simulations. This improvement in the physical accuracy of the model has allowed to study the ECR transition and the power absorption in new regions in the vicinity of the source.

The fraction of the total antenna power deposited inside the effective regions for the thrust generation in a HPT device can be affected by the power absorption in the plume and thruster surroundings.

Still, the normalized power deposition map inside the tube and near plume appears to be quite stable and not dependent on the conditions outside the thruster. The fact that the solution is mainly local in this region can be an indication of the inductive mechanism of RF power coupling in HPTs. The shorter waves traveling around outside the tube seem to affect very little the solution inside.

Even in a space environment, a faint low density plasma can envelope the thruster and the decreasing magnitude of the magnetic field guarantees that an ECR boundary will always surround the device, cutting through the plume. This feature could confine the electromagnetic power and prevent free-space losses. Nevertheless, the behavior of the electromagnetic waves can be very different for an overdense ($\omega_{pe} > \omega$) or underdense plasma ($\omega_{pe} < \omega$). Only the overdense case, corresponding to a background plasma density $n_e > 2.28 \cdot 10^{12} m^{-3}$ for 13.56 MHz excitation frequency, has been studied in the preliminary simulations. For this study case, the waves seem to mainly be reflected back at the ECR surface but that might not be the case in

a lower density plasma, as propagating modes exist beyond the ECR in underdense configurations. This investigation will be carried out in future woks.

Although the confinement in the low density surroundings of the thruster is to be investigated, the plume will always feature a transition like the one shown in the results section. Moreover, the transition can be displaced and its shape modified changing not only the background magnetic field but also the antenna excitation frequency. This fact should be consider in the future design and optimization of HPTs.

Finally, numerical convergence at lower collisionality should be solved in future simulations in order to be capable of resolving the smaller structures near the resonance while maintaining a nominal collision frequency profile. The later was scaled up by a factor 5 for this preliminary study. Improving the mesh node density in the critical areas could be achieved by increasing the computation time/resources or employing an unstructured mesh with a Finite Element (FEM) code. Though a considerable numerical noise was observed, initial simulations with nominal collisions (not reported here) have shown an even greater plume heating, even surpassing the chamber one and approaching the tube values.

7. References

[1] Ahedo, E., "Plasma Dynamics in a Helicon Thruster," *Progress in Propulsion Physics*, edited by L. T. DeLuca, C. Bonnal, O. J. Haidn, and S. M. Frolov, Vol. IV of *EUCASS Advances in Aerospace Sciences*, chap. 3, Torus Press, 2013, pp. 337–354.

[2] Takahashi, K., "Magnetic nozzle radiofrequency plasma thruster approaching twenty percent thruster efficiency," *Scientific Reports*, Vol. 11, No. 1, 2021, pp. 1–12.

[3] Tian, B., Merino, M., and Ahedo, E., "Two-dimensional plasma-wave interaction in an helicon plasma thruster with magnetic nozzle," *Plasma Sources Science and Technology*, Vol. 27, No. 11, 2018, pp. 114003.

[4] Domínguez-Vázquez, A., *Axisymmetric simulation codes for Hall effect thrusters and plasma plumes*, Ph.D. thesis, Universidad Carlos III de Madrid, Leganés, Spain, 2019.

[5] Zhou, J., Pérez-Grande, D., Fajardo, P., and Ahedo, E., "Numerical treatment of a magnetized electron fluid within an electromagnetic plasma thruster code," *Plasma Sources Science and Technology*, Vol. 28, No. 11, 2019, pp. 115004.

[6] Sánchez-Villar, A., Zhou, J., Merino, M., and Ahedo, E., "Self-consistent simulation of a coaxial ECR plasma thruster," 2020.

[7] Zhou, J., Jiménez, P., Merino, M., Fajardo, P., and Ahedo, E., "Numerical Simulations of the Plasma Discharge in a Helicon Plasma Thruster," 36th *International Electric Propulsion Conference*, No. IEPC-2019-330, Electric Rocket Propulsion Society, Vienna, Austria, 2019.

[8] Ahedo, E. and Merino, M., "Two-dimensional supersonic plasma acceleration in a magnetic nozzle," *Physics of Plasmas*, Vol. 17, No. 7, 2010, pp. 073501.

[9] Zhou, J., Sánchez-Arriaga, G., Ahedo, E., Martínez-Sánchez, M., and Ramos, J., "Collisional effects in non-stationary plasmas expansions along convergent-divergent magnetic nozzles," *Space Propulsion Conference 2018*, 00332, Association Aéronautique et Astronautique de France, Seville, Spain, 2018.

[10] Stix, T. H., *Waves in plasmas*, Springer Science & Business Media, 1992.

[11] Jin, J.-M. and Riley, D. J., *Finite element analysis of antennas and arrays*, John Wiley & Sons, 2009.

[12] Yee, K., "Numerical solution of initial boundary value problems involving Maxwell's equations in isotropic media," *IEEE Transactions on antennas and propagation*, Vol. 14, No. 3, 1966, pp. 302–307.

[13] Chen, G., Arefiev, A., Bengtson, R., Breizman, B., Lee, C., and Raja, L., "Resonant power absorption in helicon plasma sources," *Physics of Plasmas*, Vol. 13, 2006, pp. 123507.

[14] Tian, B., *Modeling of physical processes in radio-frequency plasma thrusters*, Ph.D. thesis, 2017.

[15] Kamenski, I. and Borg, G., "An evaluation of different antenna designs for helicon wave excitation in a cylindrical plasma source," *Physics of Plasmas*, Vol. 3, 1996, pp. 4396.